Analytical Tools for Point Source Interferometry

Gregory W. Hoth, Bruno Pelle, John Kitching, and Elizabeth A. Donley

NIST, 325 Broadway, Boulder, CO 80305

ABSTRACT

Light pulse atom interferometry can be used to realize high-performance sensors of accelerations and rotations. In order to broaden the range of applications of these sensors, it is desirable to reduce their size and complexity. Point source interferometry (PSI) is a promising technique for accomplishing both of these goals. With PSI, rotations are measured by detecting the orientation and frequency of spatial fringe patterns in the atomic state. These spatial fringes are primarily due to a correlation between an atom's initial velocity and its final position, which is created by the expansion of a cold atom cloud. However, the fringe patterns are also influenced by the structure of the initial atomic distribution. We summarize several methods that can be used to investigate the relationship between the spatial fringe pattern and the initial atomic distribution. This relationship will need to be understood in detail to realize an accurate gyroscope based on PSI.

Keywords: Light pulse atom interferometer, cold atom gyroscope, point source interferometry

1. INTRODUCTION

Light pulse atom interferometers (LPAIs) have achieved excellent performance as sensors of acceleration,[1,2] rotation,[3–6] gravity,[7,8] and gravity gradients.[9] So far, LPAIs have mostly been realized as large, laboratory scale experiments. In order to realize the full potential of these sensors for applications such as inertial navigation and gravimetric surveys, it is desirable to reduce the size and complexity of these systems to enable them to move outside the laboratory environment.[6,10,11] Towards this goal, we are investigating the Point Source Interferometry (PSI) technique introduced by Dickerson[12] *et al.* as an approach to realizing a compact, high performance LPAI gyroscope.

In PSI, a $\frac{\pi}{2}-\pi-\frac{\pi}{2}$ pulse sequence is applied to an expanding cloud of cold, two-level atoms, and the expanded cloud is imaged with state-selective detection.[12] With this three-pulse sequence, the initial $\frac{\pi}{2}$ pulse puts each atom into a superposition of two states with different momenta.[13] After the first pulse, there is a free expansion period of duration T_{R} which allows the two parts of the superposition to separate in space. Then, the π pulse exchanges the momentum kick between the two parts of the superposition. After a second free expansion period with duration T_{R}, the two parts of the superposition overlap again, and the final $\frac{\pi}{2}$ pulse closes the interferometer. The pulses are typically implemented with stimulated Raman transitions.[13,14] With this approach, the internal state of the atoms after the pulse sequence depends on the phase shift between the two paths the atoms can take through the interferometer. With the three-pulse sequence, both accelerations (a) and rotations (Ω) of the apparatus produce phase shifts, which are given by

$$\Phi_{\mathrm{a}} = \vec{k}_{\mathrm{eff}} \cdot \vec{a}\, T_{\mathrm{R}}^2, \tag{1}$$

$$\Phi_{\Omega} = 2\vec{k}_{\mathrm{eff}} \cdot \left(\vec{\Omega} \times \vec{v}\right) T_{\mathrm{R}}^2, \tag{2}$$

where $\vec{k}_{\mathrm{eff}}$ is the effective wave-vector for the Raman transitions, $\vec{v}$ is the velocity of the atoms, and T_{R} is the time between consecutive pulses.

In order to realize a gyroscope, we must be able to isolate the phase shift due to rotations. With PSI, this is accomplished by exploiting the correlation between an atom's initial velocity and its final position created by

E-mail: gregory.hoth@nist.gov

Slow Light, Fast Light, and Opto-Atomic Precision Metrology X, edited by Selim M. Shahriar, Jacob Scheuer, Proc. of SPIE Vol. 10119, 1011908 · © 2017 SPIE
CCC code: 0277-786X/17/$18 · doi: 10.1117/12.2247688

the expansion of the cloud. In particular, we can make the approximation $\vec{r} \approx \vec{v} T_{\mathrm{ex}}$, where $\vec{r}$ is an atom's final position and T_{ex} is the total expansion time. With this approximation, Eq. 2 becomes

$$\Phi_\Omega = \left(2T_{\mathrm{R}}^2 \left(\vec{k}_{\mathrm{eff}} \times \vec{\Omega}\right)/T_{\mathrm{ex}}\right) \cdot \vec{r} = \vec{k}_\Omega \cdot \vec{r}. \tag{3}$$

Through the cloud expansion, the velocity-dependent rotation phase shift becomes a spatial gradient in the interferometer phase described by $\vec{k}_\Omega$. This phase gradient will give rise to a spatial fringe pattern which can be detected by imaging the cloud. By measuring the frequency and orientation of the spatial fringes, we can infer two components of $\vec{\Omega}$.

Point source interferometry has several features which suggest it is a promising candidate for a compact LPAI gyroscope. The spatial fringe pattern makes it possible to isolate the rotation phase shift with only one atomic source. In other three-pulse LPAI gyroscopes, two counter-propagating sources are required to distinguish the effects of rotations and accelerations.[3,6,15,16] With PSI, the cold atom cloud does not have to be launched, which further simplifies the experimental sequence compared to other cold-atom LPAI gyroscopes. The rotational dynamic range can also be increased by the use of spatially resolved detection. Finally, PSI could enable the characterization of the wave-front aberrations of the beam used to drive the interferometer pulse sequence.[12] These aberrations are an important limitation to the long-term stability of state of the art LPAI sensors.[15,17]

However, the benefits offered by PSI come with a cost. In a real system, the correlation between the atoms' initial velocities and their final positions is not completely determined by the expansion time. It also depends on the detailed structure of the initial distribution. In previous work,[18] we have shown that the structure of the initial distribution can cause shifts in the gyroscope scale factor. Navigation grade gyroscopes are expected[19] to have a scale factor stability of a few parts-per-million (ppm), and so the initial distribution will need to be carefully controlled to realize a high-performance PSI gyroscope. If the initial distribution has a Gaussian density profile and a velocity distribution characterized by a temperature T, then the bias introduced by the initial distribution can be described as a scale factor shift. Here, we show that this is not the case for most initial distributions. Therefore, it is important to investigate other biases on the rotation measurement that can be introduced by structure in the initial distribution.

In this work, we describe several analytical tools that can be used to investigate the relationship between the initial distribution and the spatial fringe patterns. Section 2 derives an expression for the PSI signal in the point-source limit. Section 3 develops a model for the PSI fringes in the case of an initial cloud with an extended spatial distribution, $n_0(r)$, and a temperature, T, by treating the initial cloud as a collection of many point sources. The case of a cloud with a Gaussian initial density profile is considered in detail. In this case, it is possible to obtain an analytical solution for the PSI fringes that reveals several new features. Section 4 considers the spatial fringes in the Fourier domain. This picture reveals that essentially any structure in the initial distribution is expected to bias the frequency of the spatial fringes away from the point-source limit. Section 5 develops a model of the PSI fringes in phase space. This phase-space picture both provides an intuitive explanation of the effects of a finite initial cloud size and makes it possible to consider initial distributions where the velocity distribution is not described by a temperature. Finally, Section 6 summarizes the conclusions from these models.

2. THE POINT-SOURCE LIMIT

It is useful to consider the case where the atoms are initially concentrated in an infinitesimally small point source. This case is analytically tractable, and it reveals the essential physics of the PSI measurement. In this section, we will derive an expression for the density distribution of the population in one of the interferometer states after the $\frac{\pi}{2} - \pi - \frac{\pi}{2}$ pulse sequence in the point-source limit. In the following sections, we will leverage this simple case to model a cloud with a spatially extended initial distribution. To begin, consider a point source with N two-level atoms at temperature T. The atoms have a velocity distribution given by

$$p(\vec{v}) = \frac{N}{(2\pi)^{\frac{3}{2}}\,\sigma_{\mathrm{v}}^3} \exp\left(-\vec{v}^{\,2}/2\sigma_{\mathrm{v}}^2\right), \tag{4}$$

where the width of the velocity distribution is $\sigma_v = \sqrt{k_B T/m}$. At $t = 0$, the cloud begins to expand. Since the initial cloud is a point source, the position of each atom after an expansion time T_{ex} is given by $\vec{r} = \vec{v} T_{ex}$. The cloud expansion essentially maps the velocity distribution into a spatial distribution. Applying this principle to Eq. 4 gives

$$n(\vec{r}, T_{ex}) = \frac{N}{(2\pi)^{\frac{3}{2}} \sigma_{ps}^3} \exp\left(-\vec{r}^2/2\sigma_{ps}^2\right), \tag{5}$$

where $\sigma_{ps} = \sigma_v T_{ex}$ characterizes the width of the expanded point source.

As the cloud expands, a $\frac{\pi}{2} - \pi - \frac{\pi}{2}$ pulse sequence is applied. The effect of the interferometer pulse sequence is to change the internal state of the atoms. The probability for an atom to change its internal state can be described by

$$p = (1 + c\cos(\Phi))/2, \tag{6}$$

where c is the contrast and Φ is the interferometer phase shift. In the point-source limit, the rotation phase shift can be expressed as a phase gradient given by Eq. 3.

By combining Eqs. 3, 5, and 6, we obtain an expression for the final density profile of one of the interferometer states in the point-source limit. The result is

$$n_{ps}(\vec{r}, t) = \frac{N \exp\left(-\vec{r}^2/2\sigma_{ps}^2\right)}{(2\pi)^{\frac{3}{2}} \sigma_{ps}^3} \frac{\left(1 + c\cos\left(\vec{k}_\Omega \cdot \vec{r} + \phi_0\right)\right)}{2}, \tag{7}$$

where ϕ_0 is a phase offset due to other sources of interferometer phase shifts. The density distribution for the other output state has the same form with the sign of the contrast reversed.

In this derivation, we have neglected the effects of gravity and the Raman momentum kick on the motion of the atoms because neither of these effects alter the wave-vector of the spatial fringes. The effects of gravity and the Raman momentum kick during the $\frac{\pi}{2} - \pi - \frac{\pi}{2}$ pulse sequence are accounted for in the derivation of the interferometer phase shifts. If $\vec{g}$ is not parallel to $\vec{k}_{eff}$ and the cloud is allowed to fall before the beginning of the interferometer pulse sequence, then the change in the atoms' velocity due to gravity will produce a phase shift via Eq. 2. However, this phase shift will be the same for all the atoms in the cloud so it will not affect the phase gradient in Eq. 3. The Raman momentum kick and gravity do influence the final position of the atoms during detection. It is straight forward to include these effects in Eq. 7, but these details would only muddy the waters.

3. MANY POINT SOURCES—A GAUSSIAN INITIAL CLOUD

The case of an initial cloud with a density distribution $n_0(\vec{r})$ and a temperature T can be described as a collection of many point sources. The evolution of each point source during the interferometer sequence can be described by Eq. 7, and the final distribution is given by the sum of all the expanded point sources.

It is useful to begin by considering a small volume dV of the initial cloud located at a position $\vec{R}$. The number of atoms contained in this region is given by $N_i = n_0(R)\, dV$. After a time T_{ex}, the atoms from this region will have expanded into a density distribution described by $(n_0(R)\, dV)\, n_{ps}\left(\vec{r} - \vec{R}, T_{ex}\right)$ where $n_{ps}(\vec{s}, T_{ex})$ describes the profile of an expanded point source centered on $\vec{s} = 0$. The final density distribution can be obtained by integrating over all possible values of $\vec{R}$, which gives

$$n(\vec{r}, T_{ex}) = \int d^3R\; n_0(R)\, n_{ps}\left(\vec{r} - \vec{R}, T_{ex}\right) = n_0(\vec{r}) * n_{ps}(\vec{r}, T_{ex}), \tag{8}$$

where the $*$ operator represents convolution.

In order to assess the implications of a finite initial size, it is useful to consider a Gaussian initial density distribution. In this case, it is possible to evalute Eq. 8 analytically. Formally, the initial density distribution can be described by Eq. 5 with a characteristic width σ_0, and the point-source solution is described by Eq. 7. After evaluating the integral, we find that the final density distribution of each of the interferometer states is described by a Gaussian modulated by a spatial fringe as was the case for the point-source solution in Eq. 7.

However, the cloud size, the fringe frequency, and the fringe contrast are all modified. The final cloud size becomes $\sigma_f = \sqrt{\sigma_0^2 + \sigma_{\mathrm{ps}}^2}$, which is the familiar result for an expanding cloud with a Gaussian initial density profile. The spatial fringe wave-vector becomes

$$\vec{k}_{\Omega,\mathrm{g}} = \vec{k}_{\Omega,\mathrm{ps}} \left(1 - \sigma_0^2/\sigma_{\mathrm{f}}^2\right), \tag{9}$$

where $\vec{k}_{\Omega,\mathrm{ps}}$ is the expected phase gradient in the point-source limit (Eq. 3). The fringe contrast becomes

$$c(\Omega) = c_0 \exp\left(-k_{\Omega,\mathrm{ps}}^2 \sigma_0^2 \left(1 - \sigma_0^2/\sigma_{\mathrm{f}}^2\right)/2\right), \tag{10}$$

where c_0 is the interferometer contrast with $\Omega = 0$.

Looking at Eq. 9 and Eq. 10, we can see that a finite initial cloud size has two effects. It causes the spatial fringe contrast to decrease as a function of Ω, and it leads to a shift in the spatial fringe frequency. The loss of contrast can be understood by noting that when the cloud has a finite initial size, atoms with different initial velocities will end up at the same final position. Since our detection method is only sensitive to the final position of the atoms, we must average over this distribution of phase shifts, which will wash out the spatial fringes.

The velocity spread at a point in the expanded cloud can be estimated by modeling the initial cloud as a uniform ball with diameter d. The maximum velocity spread will be the difference in velocities between atoms that start on opposite sides of the initial cloud, which is given by $\delta v = d/T_{\mathrm{ex}}$. Via Eq. 2, this velocity spread corresponds to a range of phase shifts $\delta\phi = 2k_{\mathrm{eff}} T_{\mathrm{R}}^2 \Omega \delta v$. The maximum observable rotation rate roughly corresponds to $\delta\phi = 2\pi$, which leads to

$$\Omega_{\max} = \frac{\pi}{k_{\mathrm{eff}} d} \frac{T_{\mathrm{ex}}}{T_{\mathrm{R}}^2}. \tag{11}$$

The prediction of this simple model of the fringe contrast loss can be compared to the result obtained from Eq. 8 by calculating a rotation rate that characterizes the contrast loss. A convenient choice is the rotation rate where the contrast has fallen to 50 % of its initial value. For the case of a Gaussian initial cloud, Eq. 10 leads to

$$\Omega_{50\%} = \frac{\sqrt{\ln 4}}{k_{\mathrm{eff}} \sigma_0} \frac{T_{\mathrm{ex}}}{2T_{\mathrm{R}}^2} \left(1 - (\sigma_0/\sigma_{\mathrm{f}})^2\right)^{-1/2}. \tag{12}$$

Looking at Eqs. 11 and 12, we can see that these two models make similar predictions for the rotation rate that characterizes the contrast loss. In the limit $\sigma_{\mathrm{f}} \gg \sigma_0$, the two rotation rates differ by only a constant, which indicates that the simple picture of the contrast loss captures the essential physics.

Unlike the contrast loss, it is difficult to precisely identify the source of the spatial frequency shift with this picture. By evaluating the integral in Eq. 8, we added up a large number of truncated sinusoids with central frequency k_Ω and obtained a truncated sinusoid with a different central frequency k'_Ω. If we were working with the more familiar case of infinite sinusoids, this would not be possible. In the case of truncated sinusoids, it is possible for interference effects to shift the dominant frequency because each sinusoid actually contains a range of frequencies.

This interference effect can be visualized by comparing the spatial fringes from different parts of the initial cloud as shown in Fig. 1. In the left panel, each expanded point-source has a width that is equal to the initial cloud width ($\sigma_{\mathrm{ps}} = \sigma_0$). In this small expansion regime, the spatial fringes from different regions of the initial cloud are out of phase with each other. As a result, they interfere and produce a final cloud with a spatial frequency that is significantly shifted from the frequency of the individual point sources. In the right panel, the point sources have expanded to be significantly larger than the initial cloud ($\sigma_{\mathrm{ps}} = 3\sigma_0$), and so the spatial fringes from the individual point sources are more in phase with each other. As a result, the individual point sources combine to produce a cloud with a spatial frequency that is much closer to the point-source limit.

This spatial interference effect provides an explanation for the frequency shift caused by the structure of the initial distribution, but it is difficult to generalize. We can gain more insight into the connection between the spatial fringe frequency and the structure of the initial distribution by studying the spatial fringe patterns in the Fourier domain.

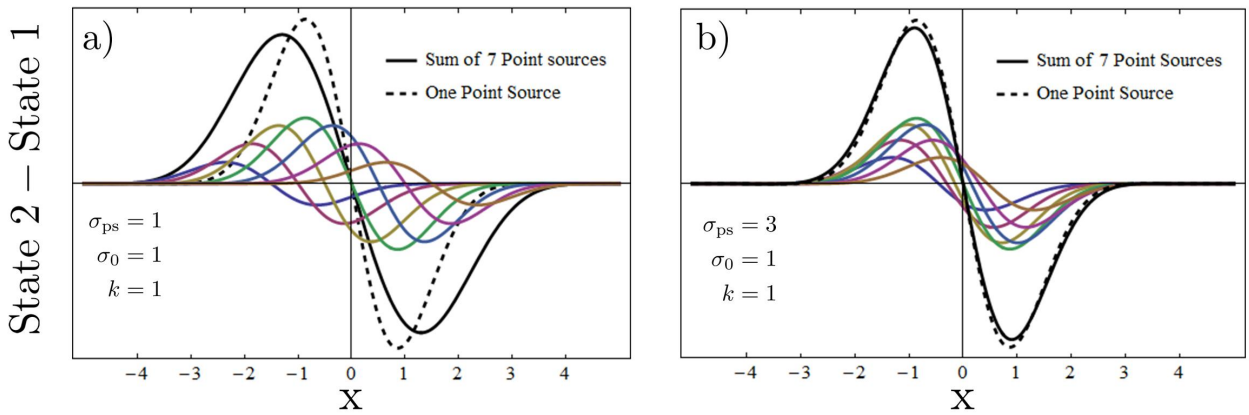

Figure 1. A visualization of the interference effect which leads to the spatial fringe frequency shift. Seven point sources (colored lines) are used to approximate the spatial fringes produced with a Gaussian initial density distribution. The number of atoms in each point source is determined by the initial cloud shape. The sum of the seven point sources (solid black line) can be compared to a single point source (dashed line). In order to emphasize the spatial fringe, we plot the difference of the density distribution for the two interferometer states, which eliminates the offset in Eq. 7. (a) The width of each point source, σ_{ps}, is equal to the initial cloud size, σ_0, which corresponds to a final cloud size $\sigma_f = \sqrt{2}\sigma_0$. In this case, the fringes from the individual point sources are out of phase with each other. When all the individual point sources are added together, the frequency of the resulting spatial fringe is clearly different than the frequency of the individual point sources. (b) $\sigma_{ps} = 3\sigma_0$, which corresponds to a final cloud size $\sigma_f = \sqrt{10}\sigma_0$. In this case, the fringes from the individual point sources are more in phase and the frequency shift is much smaller.

4. PSI FRINGES IN THE FOURIER DOMAIN

So far, we have seen that the structure of the initial distribution can bias the frequency of the detected spatial fringes away from the prediction of the point-source limit. For a Gaussian initial density distribution, this bias takes the form of a shift in the scale factor connecting the spatial fringe to the detected fringe frequency, but it is not clear if this shift is somehow unique to the case of a Gaussian cloud. In this section, we will see that frequency shifts are expected to occur with essentially any initial distribution. We will also see that it is challenging to identify a general procedure that can be used to exactly determine the rotation rate from a measurement of the spatial fringe pattern. This indicates that detailed knowledge of the initial distribution will be necessary to realize an accurate PSI gyroscope. As a first step, we will take a closer look at the fringe patterns produced by a single point source.

4.1 One Point Source

Consider the density distribution for a single point source (Eq. 7) again. For simplicity, we'll work in one dimension with perfect fringe contrast ($c = 1$) and set the total atom number $N = 1$. With these simplifications, a point source centered at position x_c expands into a density distribution given by

$$n_{ps}(x) = \frac{1}{\sqrt{2\pi}\sigma_{ps}} \exp\left(-\frac{(x - x_c)^2}{2\sigma_{ps}^2}\right) \frac{(1 + \cos(k_\Omega (x - x_c) + \phi))}{2}. \tag{13}$$

The Fourier transform of the point-source solution is given by

$$\hat{n}_{ps}(k) = \frac{e^{-ikx_c}}{\sqrt{8\pi}} \left(\exp\left(-\frac{k^2\sigma_{ps}^2}{2}\right) + \frac{e^{i\phi}}{2}\exp\left(-\frac{(k + k_\Omega)^2\sigma_{ps}^2}{2}\right) + \frac{e^{-i\phi}}{2}\exp\left(-\frac{(k - k_\Omega)^2\sigma_{ps}^2}{2}\right)\right). \tag{14}$$

The Fourier transform of the expanded point source, $\hat{n}_{ps}(k)$, has an intuitively appealing structure. It is a sum of three Gaussian peaks centered at $k = \pm k_\Omega$ and $k = 0$. Each peak has a width $\sigma_k = 1/\sigma_{ps}$, determined by the spatial width of the expanded point source. This structure is illustrated in Fig. 2a.

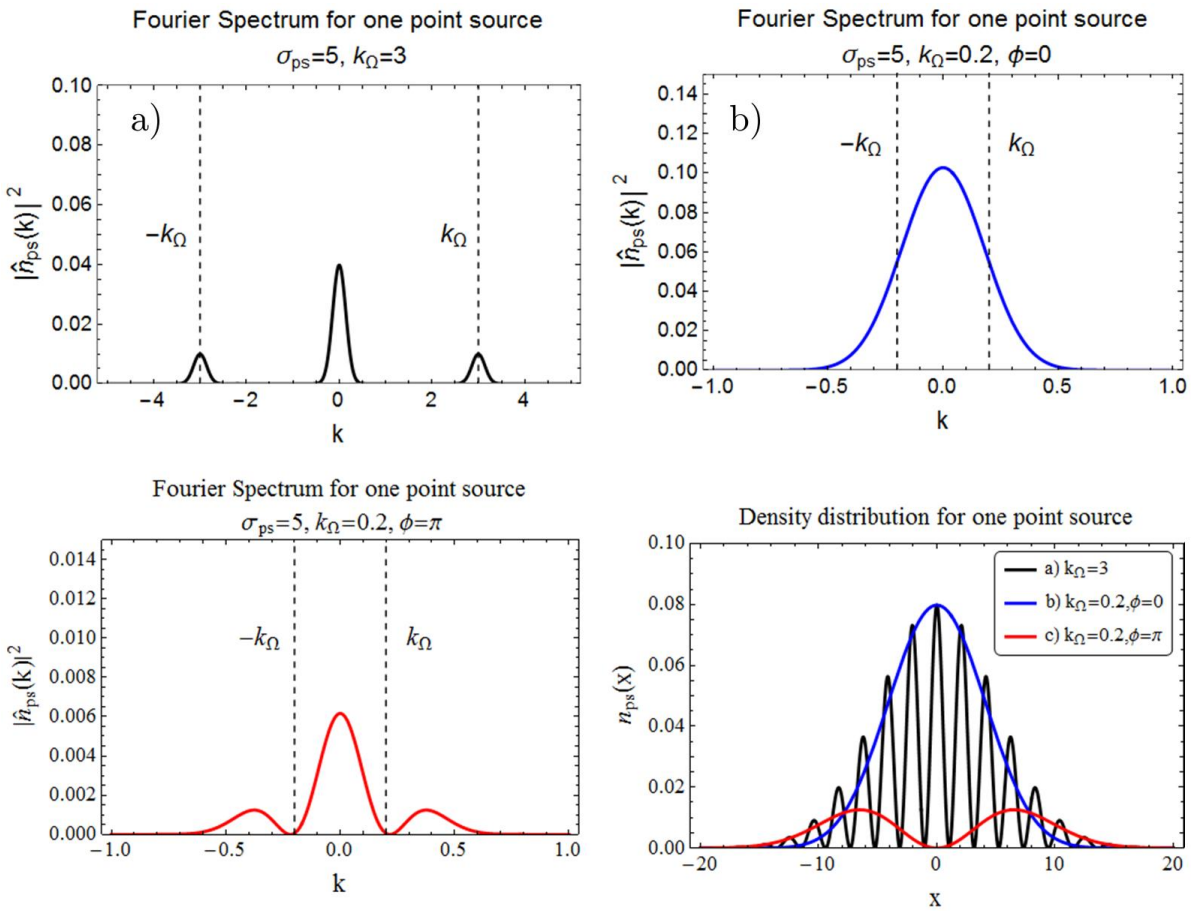

Figure 2. An illustration of the Fourier spectrum of the spatial fringes from a single point source in various cases. Panel a) illustrates a case where the spatial fringes are well resolved. The three peak structure is intuitive, but it only occurs if the spatial frequency k_Ω is sufficiently large ($k_\Omega \gg 1/\sigma_{\rm ps}$). Panels b) and c) show that when $k_\Omega \approx 1/\sigma_{\rm ps}$, the Fourier spectrum can have only one peak or even peaks at frequencies other than k_Ω, depending on the interferometer phase ϕ. Panel d) illustrates the real-space density distribution for the three cases shown panels in a) to c).

It is important to consider how we can determine the rotation rate from a measurement of the density distribution in practice. One approach is to estimate the dominant frequency in the Fourier spectrum of the imaged density distribution and convert it to a rotation rate with Eq. 3. This approach will work well as long as the point-source spatial fringe frequency satisfies $k_\Omega \gg 1/\sigma_{\rm ps}$. Physically, this corresponds to the case where one can observe several periods of the fringe pattern across the expanded cloud. In this case, the dominant frequency in the Fourier spectrum coincides with k_Ω as we intuitively expect. However, when $k_\Omega \sim 1/\sigma_{\rm ps}$, the Fourier peaks are not resolved. In this case, the Fourier spectrum can depend strongly on the interferometer phase ϕ and peaks can appear at frequencies other than $k_{\Omega,\rm ps}$ as shown in Fig. 2b,c. This makes it difficult to determine the rotation rate from the Fourier spectrum for small Ω.

In the point-source limit, we can accurately estimate the rotation rate by combining several measurements of the density distribution with different overall phases. Each point in the cloud can be described by a fringe of the form $n(x) = y_0 + A\cos(\phi_0 + \varphi(x))$, where y_0 is the fringe offset, A is the fringe amplitude, $\varphi(x)$ is the spatial phase shift, and ϕ_0 is an overall phase-shift which can be controlled experimentally. The three fringe parameters, A, y_0, and $\varphi(x)$, can be determined from three separate images of the density distribution that correspond to different overall phases. A convenient choice is the set $\phi_0 = 0$, $\frac{\pi}{2}$, and π. In this case, the spatial phase is given

by

$$\varphi(r) = \arctan\left(\frac{I_0 - I_\pi}{2I_{\pi/2} - (I_0 + I_\pi)/2}\right), \tag{15}$$

where I_ϕ refers to the image with the corresponding value of ϕ_0. For a single point source, $\varphi(x) = k_\Omega x$ with k_Ω given by Eq. 3 in all cases. However, things get more complicated if we allow even two point sources.

4.2 Two Point Sources

Consider two point sources with the same number of atoms separated by a distance x_0. Using the Fourier shift theorem, $\mathrm{F}(n(x - x_0)) = \exp(-ikx_o)\,\hat{n}(k)$, the two point-source Fourier spectrum can be expressed as

$$\hat{n}_{2\mathrm{ps}}(k) = (1 + \exp(-ikx_0))\,\hat{n}_{\mathrm{ps}}(k)\,. \tag{16}$$

It is easy to find cases where the dominant frequency in the two point-source spectrum is not k_Ω. For example, if $k_\Omega x_0 = \pi$, then $\hat{n}_{2\mathrm{ps}}(k_\Omega) = 0$. The Fourier spectrum for this case is shown as a blue curve in Fig. 3a. Note that while we have complete destructive interference at k_Ω, there are still two peaks in the Fourier spectrum on either side of k_Ω. If we were dealing with infinite sine waves, we would have perfect destructive interference and these peaks would vanish. However, because we are dealing with truncated sine waves, some oscillations remain at frequencies other than k_Ω.

We can also find cases where the Fourier spectrum is nearly a three peak spectrum, like the single point-source spectrum shown in Fig. 2a, except that the dominant frequency is not k_Ω. For example, the purple curve in Fig. 3a illustrates the case where $k_\Omega x_0 = 3.5$, and the dominant peak in the Fourier spectrum is shifted to a slightly higher frequency. A close inspection will show that there are also two small additional peaks at lower frequencies in this case.

The spatial phase for these two examples is plotted in Fig. 3c. In the case $k_\Omega x_0 = \pi$, the phase is a pure gradient with slope k_Ω except for a π phase jump at $x = 0.5$. The case with $k_\Omega x_0 = 3.5$ is more complicated. Looking at Fig. 3c, we can see $\varphi(x)$ is well approximated by a gradient with a slope slightly larger than k_Ω. However, if we subtract the expected phase gradient $k_\Omega x$, we can see that $\varphi(x)$ is actually nonlinear as shown in Fig. 3d.

It is useful to examine how these results change as the point sources expand for a longer time before detection. Formally, this corresponds to increasing σ_{ps}. In the limit $\sigma_{\mathrm{ps}} \to \infty$, we are working with the familiar case of infinite sinusoids. By adding many infinite sinusoids together, we can change the amplitude and the overall phase of the sinusoids, but the frequency of the sinusoids remains constant. Based on this limit, we can expect that as σ_{ps} increases, the dominant frequency in the Fourier spectrum and the spatially resolved phase should converge to the values that we expect for a single point source, possibly with a reduced amplitude or an overall phase shift. Figure 4 illustrates this principle for the case of $k_0 x_0 = 3.5$. In the case of $k_\Omega x_0 = \pi$, the oscillations completely vanish in the limit $\sigma_{\mathrm{ps}} \to \infty$, which is just what we expect for two sinuosoids with an equal amplitude and a π phase shift. In the case $k_\Omega x_0 = 3.5$, we see that the peak in the Fourier spectrum converges to k_Ω, and the difference between the spatially resolved phase and the expected phase gradient becomes a constant phase shift.

This two point-source model offers several new insights. First, we can see how two truncated sine waves with central frequency k can interfere to produce oscillations with a different dominant frequency, k'. The reason is that the truncated sinusoids each contain a range of frequencies and each frequency will have a different phase shift (represented by the $\exp(-ikx_0)$ factor in Eq. 16). Since each frequency component has a different phase shift, it is possible to suppress the oscillation at k while enhancing the oscillation at k'. Second, detailed knowledge of the source distribution is needed to accurately estimate Ω from a measurement of either the spatial phase or the dominant spatial frequency. We can see this by considering the variety of structure in the spatial phase and Fourier spectrum in just the examples considered so far. In the point-source limit, the spatial phase is a pure gradient, and the magnitude of the gradient is linearly related to the rotation rate. With only two point sources, both of these features disappear. If the spatial phase is approximated as a gradient, it will be important to ensure that any frequency biases introduced by non-linearities in the spatial phase are accounted for and acceptably small. One approach to minimizing these frequency biases is to ensure that the cloud expansion is sufficiently large. In the long expansion limit ($\sigma_{\mathrm{ps}} \to \infty$), we must recover the dominant frequency and spatial phase gradient predicted by the point source model.

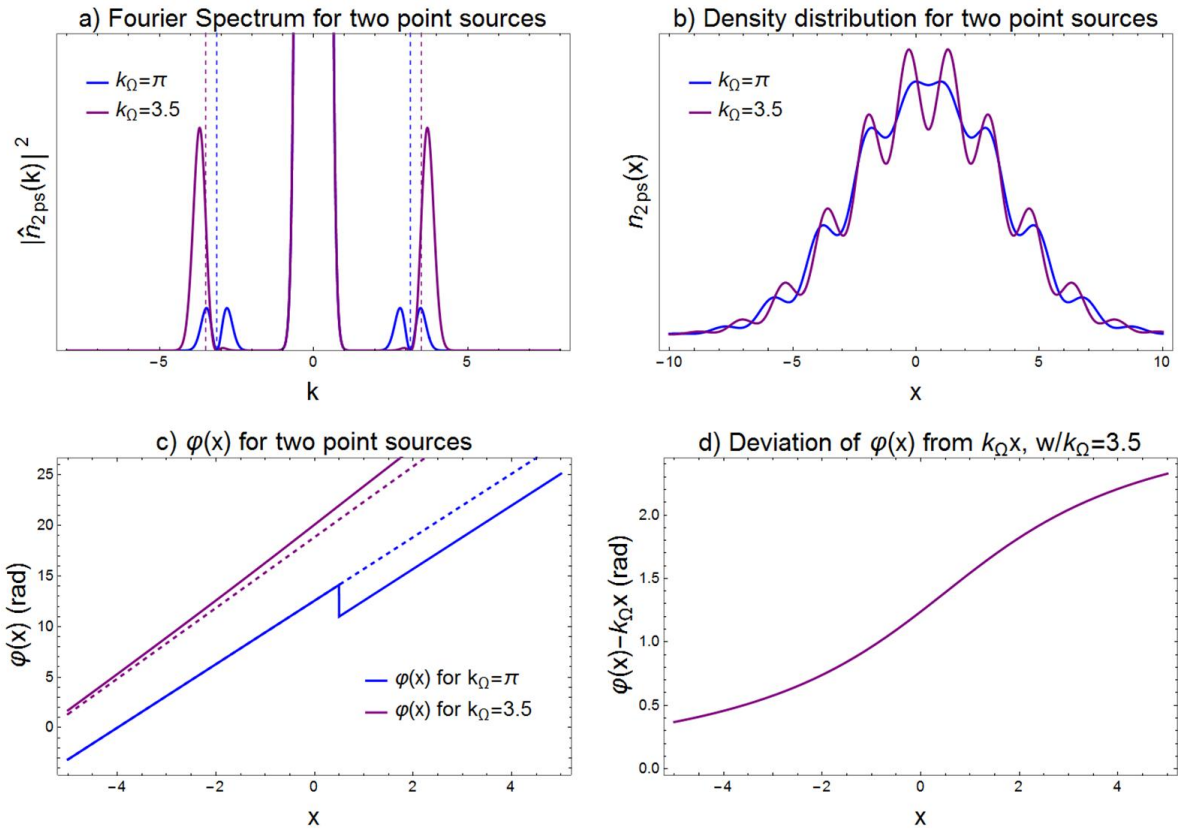

Figure 3. Examples of interference effects with two point sources. The model parameters are $\sigma_{ps} = 3$ and $x_0 = 1$. (a) Examples of the two point-source model where the dominant spatial frequency is not k_Ω. If $k_\Omega x_0 = \pi$ (blue), there is no oscillation at k_Ω at all. If $k_\Omega x_0 = 3.5$ (purple), the dominant frequency is shifted to a higher frequency. The dashed lines indicate k_Ω for these two cases. (b) Real-space density distribution for these two cases of the two point-source model. (c) Spatial phase for these two cases of the two point-source model (solid lines) compared to the phase gradient we would expect for a single point source (dashed lines). If $k_\Omega x_0 = \pi$, the spatial phase is a gradient with slope k_Ω, except for a π phase jump at $x = 0.5$. For $k_\Omega x_0 = 3.5$, the spatially resolved phase is well approximated by a gradient with a slightly higher slope than k_Ω, but a closer look reveals that the phase is no longer a pure gradient as shown in panel d). (d) $\varphi(x) - k_\Omega x$ for the case $k_\Omega x_0 = 3.5$. By examining this difference, we can see that in this case the spatial phase is no longer a pure gradient. This is also illustrated in Fig. 4.

4.3 Other Initial Density Distributions

Now we will revisit the model for an arbitrary initial density distribution. Since Eq. 8 is a convolution, its Fourier transform has the form

$$\hat{n}(k,t) = \sqrt{2\pi}\,\hat{n}_0(k)\,\hat{n}_{ps}(k,t)\,, \tag{17}$$

where $\hat{n}_0(k)$ is the Fourier transform of the initial distribution and $\hat{n}_{ps}$ is the Fourier transform of the point-source solution. Based on Eq. 17, we can expect that for any localized initial density distribution, there will be a decay of the spatial fringe contrast at large rotation rates and a shift in the frequency of the spatial fringes compared to the point-source limit. This is because any localized density distribution will have a Fourier transform that rolls off at large k so we can think of $\hat{n}_0(k)$ as slowly decaying envelope. The decreasing amplitude of $\hat{n}_0(k)$ will lead to a decay in the contrast, and the slope of the envelope will cause a shift in the central frequency of the spatial fringes. The details of the contrast decay and the spatial fringe frequency shift will depend on the initial density profile.

These general features can be illustrated by comparing two initial density profiles: a Gaussian and a box, both with full width characterized by $2\sigma_0$. The initial density distributions and their Fourier transforms are

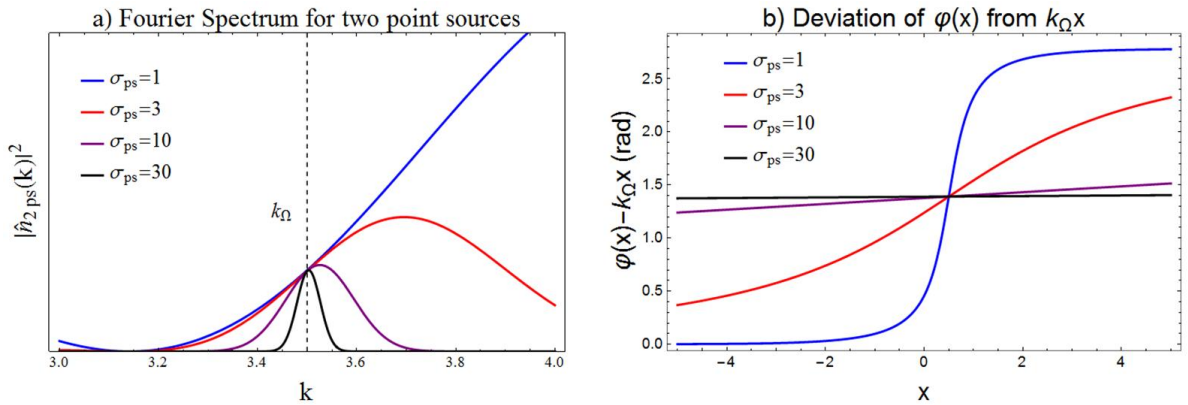

Figure 4. Effect of increasing σ_{ps} in the two point-source model with $k_\Omega = 3.5$ and $x_0 = 1$. (a) An illustration of the evolution of the spectrum as the point sources expand. The peak in the Fourier spectrum reduces in amplitude and converges to the expected frequency. (b) Difference between the spatial phase and the point-source phase gradient. As σ_{ps} increases, this difference smooths out to a constant so that the spatial phase is equal to the point-source phase gradient with an overall offset.

shown in Fig. 5a)-b). By looking at the Fourier transform of the initial density distributions, we can conclude that the contrast will decay more slowly for the box-like density distribution than the Gaussian one. We can also predict that the shifts in the central frequency of the spatial fringes will be smaller for the uniform box than for the Gaussian because the roll-off is slower.

These conclusions can be verified by examining the spatial fringe patterns produced with these initial density distributions. Two cases are illustrated in Fig. 5c)-d). In panel c), the cloud has roughly tripled in size ($\sigma_{ps} = 3\sigma_0$), and one can clearly see shifts in the dominant frequency for both initial cloud shapes. As predicted, the initially Gaussian cloud leads to a larger frequency shift and a smaller fringe contrast. In panel d), $\sigma_{ps} = 15\sigma_0$ and the dominant frequency in the spectrum cannot be distinguished from k_Ω by eye for either initial distribution.

5. PSI IN PHASE SPACE

In the previous two sections, we have modeled the PSI fringes produced by a cloud with a finite initial size by breaking the initial distribution down into many point sources. With this approach, we've identified two main effects of the initial distribution. First, the spatial fringe contrast will decrease as a function of Ω. Second, the dominant frequency of the spatial fringes for a given Ω will be shifted from the frequency calculated in the point-source limit (Eq. 3). So far, we have explained this frequency shift as a consequence of the interference of truncated sinusoids. This picture has allowed us to build some useful mathematical formalism, but it is also rather abstract. It is important to note that all of the models presented so far assume the velocity distribution of the atoms can be characterized by a uniform temperature.

We can gain more insight into the origins of the frequency shift by tracking the distribution of the atoms in both position and velocity. This distribution is often called the phase-space density $\rho(x, v)$. In this section, we will develop an alternative perspective on the PSI fringes by studying how the phase-space density evolves as the cloud expands. The first step is to derive an evolution equation for ρ. When the cloud is freely expanding, the velocity of each individual atom is constant. In a time dt, each atom moves a distance $dx = vdt$. Thus, we have $\rho\,(x + vdt, v, t + dt) = \rho\,(x, v, t)$. After expanding ρ to first order, we find that

$$\frac{\partial \rho}{\partial t} = -v\frac{\partial \rho}{\partial x}, \tag{18}$$

which has solutions of the form $\rho(x, v, t) = f(x - vt)$. In particular, if $\rho_0(x, v)$ describes the phase-space density at $t = 0$, then at future times

$$\rho(x, v, t) = \rho_0(x - vt, v)\,. \tag{19}$$

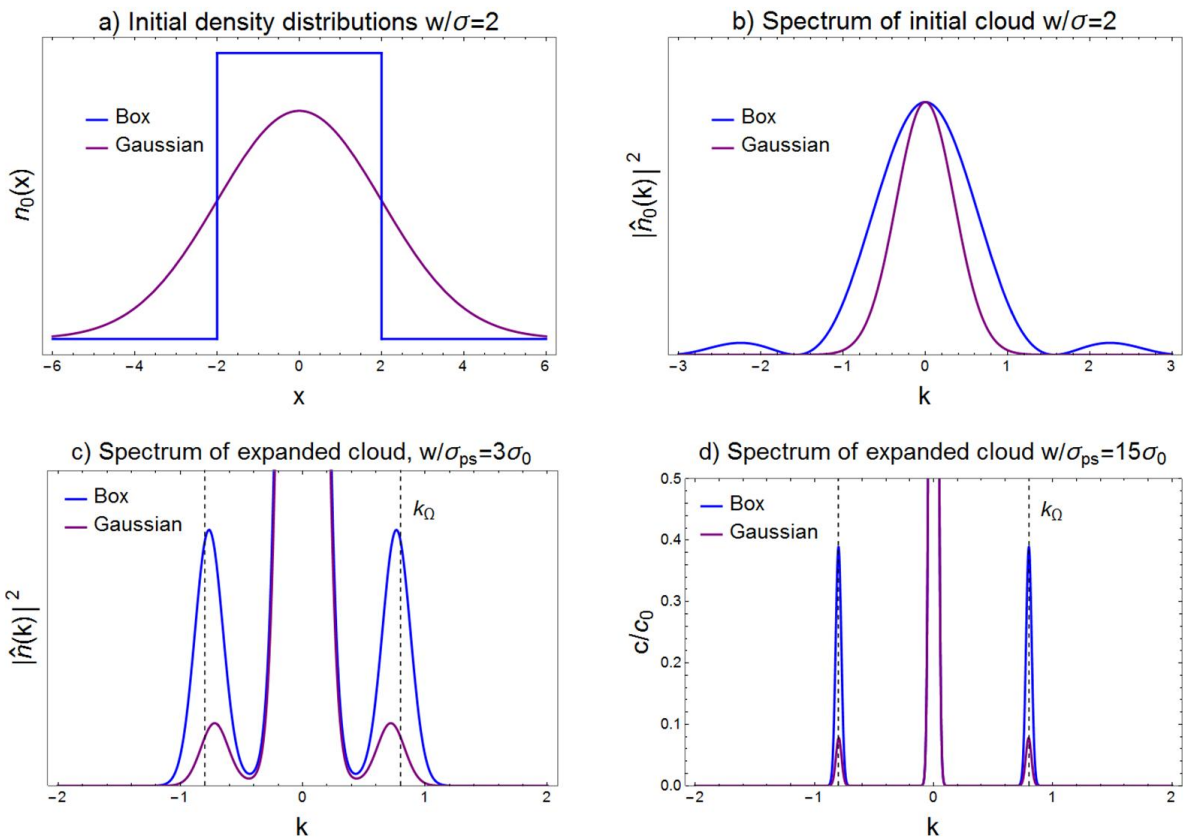

Figure 5. A comparison of the spatial fringes produced with a box-shaped initial cloud and a Gaussian initial cloud with parameters $\sigma_{\rm ps} = 2$ and $k_\Omega = 0.8$. Panel a) shows the initial density distributions. Both are normalized to have area 1. The rectangle has a diameter of $d = 2\sigma_0$. Panel b) shows the Fourier spectrum of these initial distributions. According to Eq. 17, the Fourier spectrum of the initial density distribution can be thought of as a filter acting on the point source spectrum. Panels c) and d) show examples of the Fourier spectrum of the expanded cloud for these two initial density distributions. In panel c), $\sigma_{\rm ps} = 3\sigma_0$ so the cloud has roughly tripled in size. For both initial cloud profiles, the dominant frequency is clearly shifted from k_Ω, but the frequency shift is smaller for the box-like distribution. In panel d), $\sigma_{\rm ps} = 15\sigma_0$, and the dominant frequency cannot be distinguished from k_Ω by eye.

The phase space density for one of the interferometer states can be found by multiplying ρ by the probability for an atom to occupy that state. This leads to

$$\rho_{\rm e}(x, v, t) = \rho_0(x - vt, v)\,\frac{1 + c\cos\left(2k_{\rm eff} v \Omega T_{\rm R}^2 + \phi_0\right)}{2}, \tag{20}$$

where $\rho_{\rm e}$ is the phase-space density for atoms in state $|{\rm e}\rangle$. The density distribution at time t can be found by integrating over all velocities

$$n(x, t) = \int dv\, \rho(x, v, t)\,. \tag{21}$$

So far, this is more mathematical abstraction. The real power of this approach comes from visualizing the geometry of phase space. This is typically done by plotting position on the horizontal axis and velocity on the vertical axis. With this approach, the expansion of the cloud can be visualized by noting that atoms in the upper half of the plane move to the right, and the atoms in the lower half of the plane move to the left. At $t = 0$, a point source is represented by a vertical line. At future times, the point-source phase-space density remains a straight line described by $v = x/T_{\rm ex}$, which corresponds to a perfect correlation between the atoms' position and their velocity. The cloud expansion causes the line to rotate in the $x - v$ plane.

When the cloud has a finite initial size, its initial phase-space density can be visualized as a blob that is roughly symmetric around the origin. The cloud expansion stretches the initial phase-space blob horizontally. Since phase-space volume is conserved, this stretching also causes the phase-space density to thin out vertically so that it tends to become like a long thin cigar. This thinning out of the phase-space distribution corresponds to the build up of the correlation between the atoms' final position and their initial velocity. The expansion of the cloud in phase-space is illustrated for both a point source and a cloud with a Gaussian initial density distribution and a temperature T in Fig. 6. The lower half of the figure illustrates the distribution of interferometer phase shifts and the detected fringes. In these phase-space pictures, the interferometer phase shift is constant along horizontal lines because the phase shift depends only on the atoms' velocity and not their position.

By comparing the phase-space distribution for the Gaussian cloud to the distribution for a point-source, we can see two effects of a finite initial size. First, the Gaussian cloud has a range of velocities at every point. As we saw in Sec. 3, this blurring of the correlation between the atoms' position and their velocity tends to reduce the contrast of the spatial fringes. Second, the expanded Gaussian cloud is tilted at a different angle than the point-source phase-space distribution. This tilt indicates that the average velocity is lower for the Gaussian initial cloud then we would expect based on the point-source limit. With the phase-space formalism, it is straightforward to calculate the average velocity at a given position for the Gaussian cloud case. The result is

$$v_{\mathrm{avg}}(x) = \left(1 - \frac{\sigma_0^2}{\sigma_f^2}\right) v_{\mathrm{ps}}, \tag{22}$$

where $v_{\mathrm{ps}} = x/T_{\mathrm{ex}}$ is the velocity the atoms would have if the cloud were a point source. For the Gaussian cloud, this reduction in the average velocity corresponds exactly to the shift in the spatial fringe frequency we first calculated in Eq. 9. With this perspective, we can see that the spatial frequency shift is fundamentally due to the imperfect correlation between the atoms' initial velocity and their final position.

6. CONCLUSION

We have described three pictures that can be used to quantify the relationship between the initial atomic distribution and the detected spatial fringe patterns. In the first picture, the final density distribution is calculated as the convolution of the initial density distribution with the point-source solution. This space-domain approach can yield exact solutions for a few initial distributions, and it is a useful tool for studying the implications of particular density profiles, but it is difficult to draw general conclusions about the relationship between the initial distribution and the fringe pattern with this approach. In the second picture, we consider the detected density distribution in the Fourier domain. With this picture, the Fourier transform of the initial density distribution can be thought of as a transfer function which filters the point-source solution. This picture revealed that frequency shifts are expected for essentially any localized initial distribution. The case of a Gaussian initial cloud is somewhat special because the frequency shift takes the form of a scale factor shift, and the spatial phase is expected to be a pure gradient. This will not be the case for most initial distributions. In the third picture, we consider the phase space density. By tracking the distribution of the atoms in both position and velocity, we can see that the spatial fringe frequency shift comes about because the atom's final position is an imperfect proxy for their initial velocity.

In order to realize a high performance, PSI gyroscope, these finite size effects will have to be understood and controlled with excellent precision and stability. One approach would be to use an optical trap to control the initial atomic distribution.[20] Despite the challenges posed by these finite size effects, we believe the advantages offered by the PSI technique indicate that this route to a compact, cold-atom LPAI gyroscope is worth pursuing.

ACKNOWLEDGMENTS

This work was funded by NIST. NIST is a US government agency and this work is not subject to copyright.

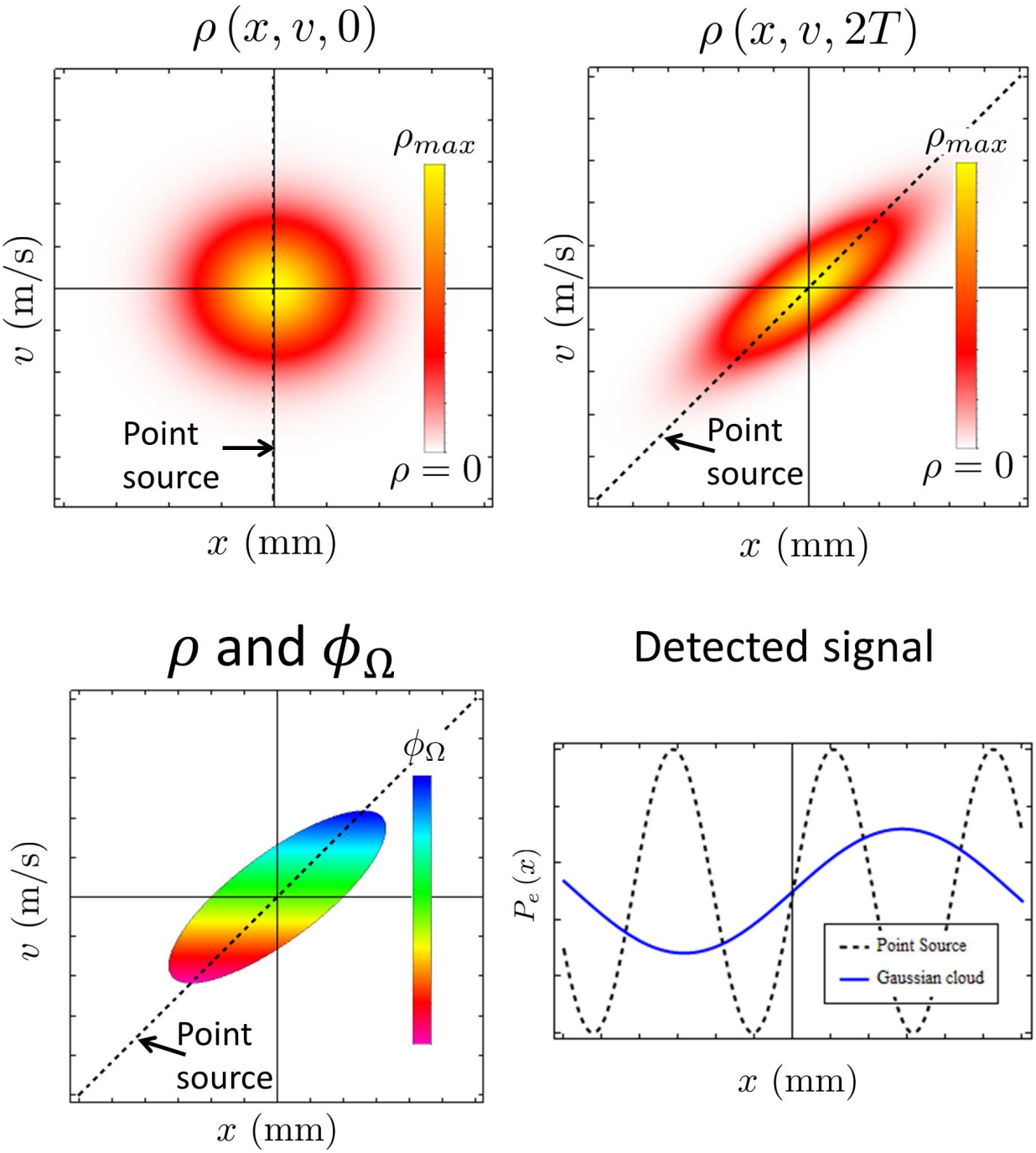

Figure 6. An illustration of the phase space picture of the PSI fringes. (Top left) The initial phase-space density for a point source (dashed line) and a Gaussian cloud. (Top right) Phase-space density for the point source and the Gaussian cloud after a time $T_{\rm ex}$. The point-source phase-space density simply rotates, but the phase-space density for the Gaussian cloud elongates and thins out. (Bottom left) Phase-space distribution colored with the interferometer phase. Detection corresponds to averaging over the vertical velocity axis. (Bottom right) Detected spatial fringes in the point source and Gaussian cloud cases.

REFERENCES

[1] McGuinness, H. J., Rakholia, A. V., and Biedermann, G. W., "High data-rate atom interferometer for measuring acceleration," *Applied Physics Letters* **100**, 011106 (Jan. 2012).

[2] Lautier, J., Volodimer, L., Hardin, T., Merlet, S., Lours, M., Pereira Dos Santos, F., and Landragin, A., "Hybridizing matter-wave and classical accelerometers," *Applied Physics Letters* **105**, 144102 (Oct. 2014).

[3] Gustavson, T. L., Landragin, A., and Kasevich, M. A., "Rotation sensing with a dual atom-interferometer Sagnac gyroscope," *Classical and Quantum Gravity* **17**, 2385–2398 (June 2000).

[4] Barrett, B., Geiger, R., Dutta, I., Meunier, M., Canuel, B., Gauguet, A., Bouyer, P., and Landragin, A., "The Sagnac effect: 20 years of development in matter-wave interferometry," *Comptes Rendus Physique* **15**, 875–883 (Dec. 2014).

[5] Berg, P., Abend, S., Tackmann, G., Schubert, C., Giese, E., Schleich, W., Narducci, F., Ertmer, W., and Rasel, E., "Composite-Light-Pulse Technique for High-Precision Atom Interferometry," *Physical Review Letters* **114**, 063002 (Feb. 2015).

[6] Rakholia, A. V., McGuinness, H. J., and Biedermann, G. W., "Dual-Axis High-Data-Rate Atom Interferometer via Cold Ensemble Exchange," *Physical Review Applied* **2**, 054012 (Nov. 2014).

[7] Merlet, S., Bodart, Q., Malossi, N., Landragin, A., Santos, F. P. D., Gitlein, O., and Timmen, L., "Comparison between two mobile absolute gravimeters: optical versus atomic interferometers," *Metrologia* **47**(4), L9 (2010).

[8] Hu, Z.-K., Sun, B.-L., Duan, X.-C., Zhou, M.-K., Chen, L.-L., Zhan, S., Zhang, Q.-Z., and Luo, J., "Demonstration of an ultrahigh-sensitivity atom-interferometry absolute gravimeter," *Physical Review A* **88**, 043610 (Oct. 2013).

[9] Biedermann, G. W., Wu, X., Deslauriers, L., Roy, S., Mahadeswaraswamy, C., and Kasevich, M. A., "Testing gravity with cold-atom interferometers," *Physical Review A* **91**, 033629 (Mar. 2015).

[10] Hauth, M., Freier, C., Schkolnik, V., Senger, A., Schmidt, M., and Peters, A., "First gravity measurements using the mobile atom interferometer GAIN," *Applied Physics B* **113**, 49–55 (Apr. 2013).

[11] Battelier, B., Barrett, B., Fouché, L., Chichet, L., Antoni-Micollier, L., Porte, H., Napolitano, F., Lautier, J., Landragin, A., and Bouyer, P., "Development of compact cold-atom sensors for inertial navigation," *Proceedings of SPIE, Quantum Optics* **9900**, 990004 (Apr. 2016).

[12] Dickerson, S. M., Hogan, J. M., Sugarbaker, A., Johnson, D. M. S., and Kasevich, M. A., "Multiaxis Inertial Sensing with Long-Time Point Source Atom Interferometry," *Physical Review Letters* **111**, 083001 (Aug. 2013).

[13] Kasevich, M. and Chu, S., "Atomic interferometry using stimulated Raman transitions," *Physical Review Letters* **67**, 181–184 (July 1991).

[14] Bordé, C. J., "Atomic interferometry with internal state labelling," *Physics Letters A* **140**, 10–12 (Sept. 1989).

[15] Gauguet, A., Canuel, B., Lévèque, T., Chaibi, W., and Landragin, A., "Characterization and limits of a cold-atom Sagnac interferometer," *Physical Review A* **80**, 063604 (Dec. 2009).

[16] Tackmann, G., Berg, P., Abend, S., Schubert, C., Ertmer, W., and Rasel, E. M., "Large-area Sagnac atom interferometer with robust phase read out," *Comptes Rendus Physique* **15**, 884–897 (Dec. 2014).

[17] Schkolnik, V., Leykauf, B., Hauth, M., Freier, C., and Peters, A., "The effect of wavefront aberrations in atom interferometry," *Applied Physics B* **120**, 311–316 (June 2015).

[18] Hoth, G. W., Pelle, B., Riedl, S., Kitching, J., and Donley, E. A., "Point source atom interferometry with a cloud of finite size," *Applied Physics Letters* **109**, 071113 (Aug. 2016).

[19] Durfee, D. S., Shaham, Y. K., and Kasevich, M. A., "Long-Term Stability of an Area-Reversible Atom-Interferometer Sagnac Gyroscope," *Physical Review Letters* **97**, 240801 (Dec. 2006).

[20] Grimm, R., Weidemüller, M., and Ovchinnikov, Y. B., "Optical Dipole Traps for Neutral Atoms," in [*Advances In Atomic, Molecular, and Optical Physics*], Walther, B. B. and Walther, H., eds., **42**, 95–170, Academic Press (2000).